JACS
JOURNAL OF THE AMERICAN CHEMICAL SOCIETY
pubs.acs.org/JACS
Communication

Nanoscale Metal–Organic Frameworks Stabilize Bacteriochlorins for Type I and Type II Photodynamic Therapy

Taokun Luo,[§] Kaiyuan Ni,[§] August Culbert, Guangxu Lan, Zhe Li, Xiaomin Jiang, Michael Kaufmann, and Wenbin Lin*

Cite This: J. Am. Chem. Soc. 2020, 142, 7334–7339
Read Online
ACCESS | Metrics & More | Article Recommendations | Supporting Information

ABSTRACT: Herein we report the design of a bacteriochlorin-based nanoscale metal–organic framework, Zr-TBB, for highly effective photodynamic therapy via both type I and type II mechanisms. The framework of Zr-TBB stabilizes 5,10,15,20-tetra(*p*-benzoato)bacteriochlorin (TBB) ligands toward oxygen and light via geometrical constraint. Upon 740 nm light irradiation, Zr-TBB efficiently generates various reactive oxygen species, including singlet oxygen, superoxide anion, hydrogen peroxide, and hydroxyl radicals, to afford superb antitumor efficacy on mouse models of breast and colon cancers, with cure rates of 40% and 60%, respectively.

Photodynamic therapy (PDT) is a minimally invasive and effective local therapy for many cancers,[1−5] but its clinical utility is limited by side effects from photosensitivity caused by residual photosensitizers (PSs) in normal tissues, shallow light penetration depth in tumors, and low oxygen concentrations in hypoxic tumors.[6−8] As highly reduced derivatives of porphyrins and chlorins, bacteriochlorins possess several distinct features to overcome the challenges faced by conventional PSs: (1) weak absorption in the visible spectrum minimizes photosensitivity from ambient light, (2) strong absorption in the near-infrared region (700−850 nm) increases PDT efficacy, and (3) type I PDT tolerates hypoxia.[9−11] Padeliporfin, a Pd-coordinated bacteriochlorin, was approved in Europe for PDT treatment of prostate cancer.[12] However, bacteriochlorins are unstable toward oxygen and light,[13−15] significantly reducing their potency in PDT.[16−18]

With tunable and porous structures,[19−22] high PS loading,[23] and rigid structures,[24] nanoscale metal–organic frameworks (nMOFs) have emerged as novel nanophotosensitizers for PDT.[25−28] By incorporating different PS ligands, nMOFs can be fine-tuned to optimize PDT efficacy. The rigid frameworks of nMOFs not only constrain the ligands from structural changes to reduce unimolecular photodecomposition but also isolate the PSs from each other to prevent inter-PS self-quenching.

Herein we report the use of nMOFs to stabilize bacteriochlorins for effective PDT. Experimental and computational studies demonstrated the stabilization of 5,10,15,20-tetra(*p*-benzoato)bacteriochlorin (TBB) ligands in the Zr-TBB nMOF toward oxygen and light owing to geometrical constraint by the framework. Zr-TBB mediated effective PDT via both type I and type II mechanisms by generating various reactive oxygen species (ROSs), including superoxide anions (O_2^-), hydrogen peroxide (H_2O_2), hydroxyl radicals ($^{\bullet}OH$), and singlet oxygen ($^1O_2$), upon irradiation at 740 nm (Scheme 1). Zr-TBB showed superb *in vivo* antitumor efficacy on 4T1- and MC38-bearing mouse models of breast and colon cancers to afford cure rates of 40% and 60%, respectively.

Scheme 1. Stabilization of Bacteriochlorin Ligands in Zr-TBB for Type I and Type II PDT

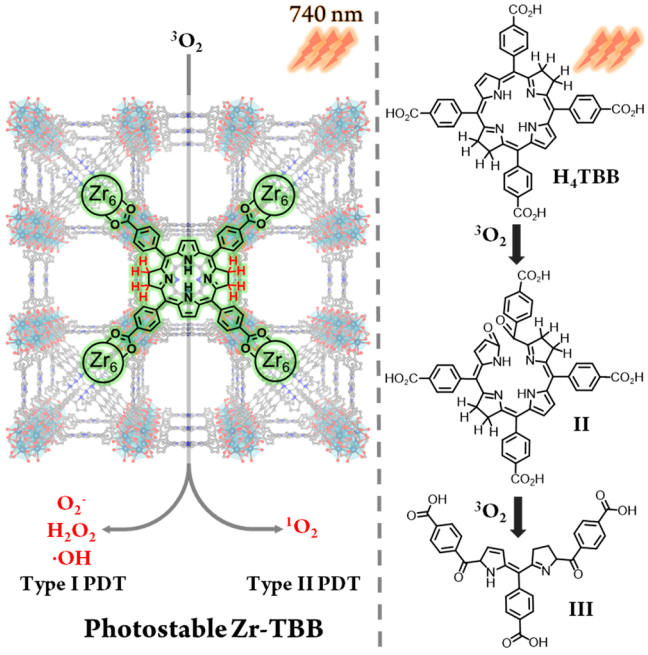

Received: February 22, 2020
Published: April 4, 2020

https://dx.doi.org/10.1021/jacs.0c02129
J. Am. Chem. Soc. 2020, 142, 7334–7339

The new bacteriochlorin H_4TBB was synthesized via solvent-free reduction of 5,10,15,20-tetra(*p*-benzoato)-porphyrin (H_4TBP) with *p*-toluenesulfonyl hydrazide (Figure S1).[29] The UV−vis spectrum of H_4TBB in *N*,*N*-dimethylformamide (DMF) exhibited four major peaks (Figure 1e)

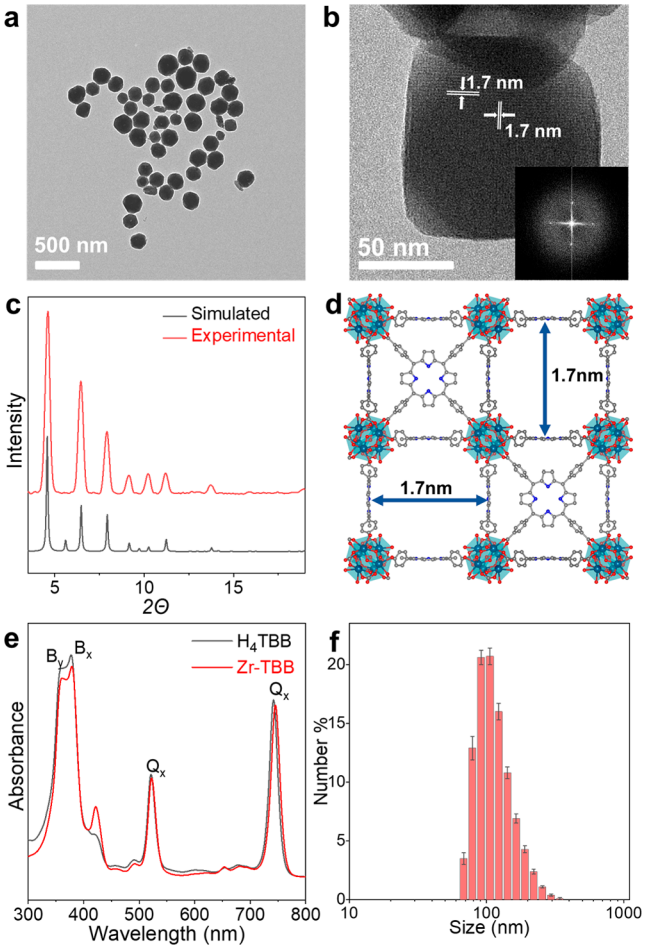

Figure 1. TEM image (a), HR-TEM image and FFT pattern (inset) (b), PXRD pattern (c), X-ray crystal structure (d), UV−vis spectra in DMF (e), and DLS number-averaged diameter in EtOH (f) of Zr-TBB.

assignable to the transitions from two HOMOs (HOMO−1 and HOMO) to two LUMOs (LUMO and LUMO+1) based on a four-orbital model.[30] For H_4TBB, the B_y peak at λ_{max} = 361 nm had a molar extinction coefficient (ε) of 70.4 $mM^{-1}\cdot cm^{-1}$, whereas the B_x peak at λ_{max} = 377 nm had an ε of 73.4 $mM^{-1}\cdot cm^{-1}$. These ε values are ∼4 times lower than those of Soret bands in H_4TBP (ε_{420} = 460 $mM^{-1}\cdot cm^{-1}$) and 5,10,15,20-tetra(*p*-benzoato)chlorin (H_4TBC, ε_{420} = 381 $mM^{-1}\cdot cm^{-1}$), suggesting that H_4TBB might alleviate photosensitivity side effects from ambient light.[26] The Q_x and Q_y peaks of H_4TBB had an ε_{521} of 32.4 $mM^{-1}\cdot cm^{-1}$ and an ε_{742} of 58.4 $mM^{-1}\cdot cm^{-1}$, respectively. The Q_y peak of H_4TBB at 742 nm is nearly ideal for tissue penetration, and H_4TBB has ∼12 and ∼2 times higher ε values than those of H_4TBP and H_4TBC, respectively.[26] H_4TBB is thus a superior PS over H_4TBP and H_4TBC, with an optimal Q_y wavelength and a much higher ε.[31]

Zr-TBB was synthesized via a solvothermal reaction of $ZrCl_4$, H_4TBB, and 88% formic acid in DMF at 100 °C under anaerobic conditions. Single-crystal X-ray diffraction of Hf-TBB revealed a PCN-224 structure in the $Im\bar{3}m$ space group with $Hf_6(\mu_3\text{-}O)_4(\mu_3\text{-}OH)_4$ secondary building units linked by TBB ligands to afford a 3-D framework of *she* topology (Figure 1d and Figure S3).[32] Powder X-ray diffraction pattern (PXRD) studies indicated that Zr-TBB adopted the same structure as Hf-TBB (Figure 1c), with a formula of $[Zr_6(\mu_3\text{-}O)_4(\mu_3\text{-}OH)_4(OH)_6(H_2O)_6]_2(TBB)_3$. Inductively coupled plasma mass spectrometry (ICP-MS) and UV−vis spectra gave a Zr-to-TBB ratio of 4.22, which is slightly lower than the theoretical ratio of 4, likely due to minor decomposition of TBB ligands during nMOF synthesis. Thermogravimetric analysis showed a weight loss of 65.9% in the 25−600 °C range, consistent with the expected value of 64.3% for the conversion of Zr-TBB to ZrO_2 (Figure S6).

Dynamic light scattering (DLS) of Zr-TBB revealed a number-averaged size of 117.9 ± 1.4 nm, with a polydispersity index of 0.09 (Figure 1f). Transmission electron microscopy (TEM) imaging (Figures 1a,b, S4, and S5) revealed spherical to cubic morphology for Zr-TBB with a diameter of approximately 100 nm. High-resolution TEM (HR-TEM) imaging gave a lattice spacing of 1.7 nm (Figure 1b) for Zr-TBB, while the fast Fourier transform (FFT) patterns (Figure 1b inset) revealed tetragonal symmetry, consistent with projection down to the crystallographic axis (Figure 1d). Additionally, the UV−vis spectrum of Zr-TBB showed the same number of peaks as H_4TBB, with the appearance of a small TBC Soret peak at ∼422 nm due to slight oxidation of TBB (4%) during nMOF synthesis.

Photostability of H_4TBB and Zr-TBB was tested in air-saturated DMF at a 5 μM TBB concentration at 740 nm (100 $mW\cdot cm^{-2}$). After irradiation for 5 min, the Q_y peak absorbance of H_4TBB dropped to <4% of the original value, indicating its severe photobleaching (Figure 2a). In contrast, Zr-TBB retained 73% and 65% of the Q_y peak absorbance after light irradiation for 15 and 30 min, respectively, indicating its much enhanced photostability over H_4TBB. The photodecomposition quantum yield of Zr-TBB (Φ_{pd} = 8.14 × 10^{-4}) was 14 times lower than that of H_4TBB (Φ_{pd} = 1.15 × 10^{-2}, Table S2). The improved TBB stability of Zr-TBB can be attributed to the spatial constraint of the nMOF framework, which prevents TBB from undergoing structural changes before photooxidation can occur, and the site isolation effect of Zr-TBB, which prevents TBB ligands from biomolecular decomposition.[33] We found the photostability of Zr-TBB and H_4TBB was much improved in oxygen-free conditions (Figure S7).

We used high-resolution mass spectrometry (HR-MS) to characterize the photobleaching products of Zr-TBB and H_4TBB after 740 nm irradiation (100 $mW\cdot cm^{-2}$) in air-saturated DMF for 4 h. Photoirradiated Zr-TBB was digested with 10% H_3PO_4 in DMSO before HR-MS analysis. For H_4TBB, the $[H_4TBB+H^+]$ peak at m/z = 795.2 disappeared, with the appearance of $[M+H^+]$ at m/z = 563.5 assignable to (*Z*)-4-(2-((5-(4-carboxy-benzoyl)-1*H*-pyrrol-2-yl)(4-carboxyphenyl)methylene)-3,4-dihydro-2*H*-pyrrole-5-carbonyl)benzoic acid (**III**, Scheme 1), a known fragmentation product from bacteriochlorin photobleaching.[34] The fragmentation of H_4TBB during photooxidation was supported by the UV−vis spectrum, which showed two new peaks at 327 and 406 nm for **III** and disappearance of all peaks corresponding to H_4TBB (Figure S7e). In contrast, only H_4TBC at m/z = 793.3 ($[M+H^+]$) was recovered from the digested photoirradiated

https://dx.doi.org/10.1021/jacs.0c02129
J. Am. Chem. Soc. 2020, 142, 7334−7339

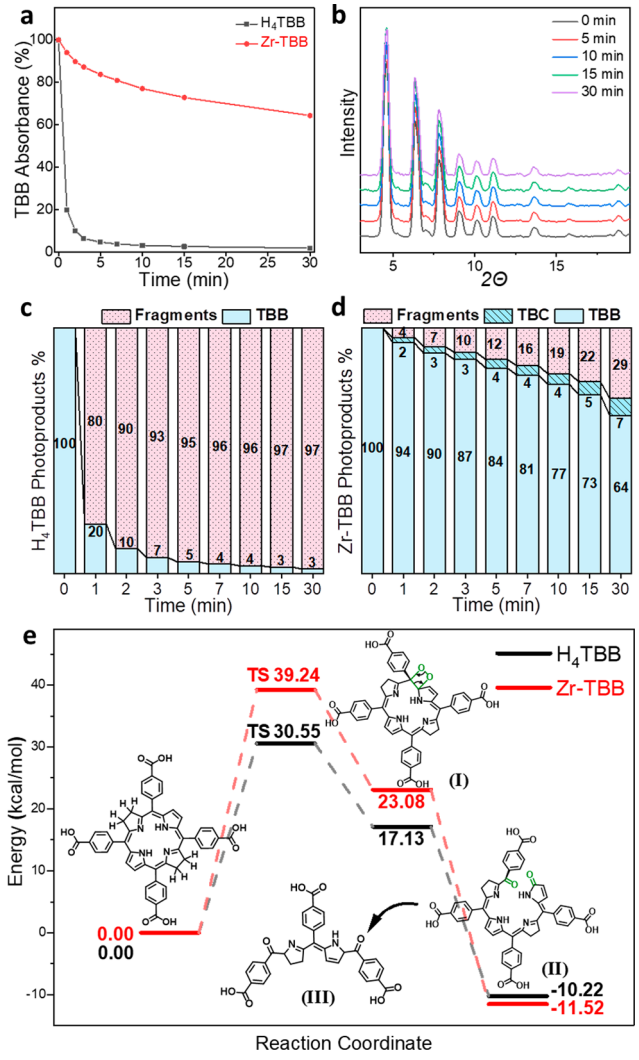

Figure 2. (a) Time-dependent TBB UV−vis absorbance after light irradiation in air-saturated DMF. (b) Time-dependent PXRD patterns of Zr-TBB after light irradiation. Percentages of photoproducts (TBB, TBC, fragments) of H_4TBB (c) and Zr-TBB (d) throughout 30 min of light irradiation. (e) Energy profiles of TBB photofragmentation in H_4TBB and Zr-TBB calculated by DFT.

Zr-TBB, with no evidence of known photofragments. TBC can be generated by direct oxidation of the pyrroline ring of TBB without significant structural changes on the bacteriochlorin.

UV−vis spectroscopy was used to quantify photobleaching products of H_4TBB (Figure 2c) and Zr-TBB (Figure 2d) after light irradiation for 1−30 min (Figure S7a,b). H_4TBB was nearly completely photobleached (95%) within 5 min to generate mostly fragmentation product **III** (95%) and a negligible amount of H_4TBC (<0.1%). In contrast, Zr-TBB retained 84% TBB in 5 min with the formation of 4% TBC. Only 12% of TBB decomposed into unknown photoproducts. As TBC is also a good PS, TBB retained 80% and 74% PDT efficacy after light irradiation for 15 and 30 min, respectively. The photostability of Zr-TBB was supported by the maintenance of crystallinity, as determined by PXRD (Figure 2b).

Photobleaching of bacteriochlorins typically starts with [2+2] peroxidation reaction between C=C double bonds and O_2 (Figure 2e).[35] The peroxidized intermediate **I** breaks the π-conjugated bacteriochlorin ring and converts sp^2-carbons into sp^3-carbons, leading to significant distortion from the planar structure of TBB. The peroxide bridge is cleaved into two ketones in intermediate **II** via retro-[2+2] cyclization. Successive peroxidation and retro-[2+2] cyclization form fragmentation product **III**. However, the rigid framework of Zr-TBB prohibits TBB ligands from undergoing large structural changes, shutting down the light-mediated peroxidation pathway. The pyrroline rings of the bacteriochlorin can still be oxidized to form TBC ligands without disturbing π-conjugation.

Density functional theory (DFT) calculations were performed to support the photostability difference of bacteriochlorins in H_4TBB and Zr-TBB (Figure 2e). The crystal structure of Zr-TBB was used, and the structures of the carboxylate groups were frozen during DFT optimization to mimic spatial constraints in the nMOF. In the calculated energy profiles, H_4TBB displayed a $\Delta G^{\ddagger}$ of 30.6 kcal/mol (1.33 eV), while the constrained TBB in Zr-TBB exhibited a much higher $\Delta G^{\ddagger}$ of 39.2 kcal/mol (1.70 eV). The 1.69 eV energy in the 740 nm light source was thus sufficient to overcome the $\Delta G^{\ddagger}$ in H_4TBB but insufficient to overcome the $\Delta G^{\ddagger}$ in Zr-TBB, which explains the resistance of Zr-TBB to peroxidation and photofragmentation.

Bacteriochlorins can generate multiple ROSs via both type I ($O_2^{\bullet-}$, H_2O_2, and $^{\bullet}OH$) and type II ($^1O_2$) mechanisms.[36] The generation of $O_2^{\bullet-}$, H_2O_2, $^{\bullet}OH$, and $^1O_2$ by H_4TBB and Zr-TBB was confirmed by electron paramagnetic resonance, hydrogen peroxide detection kit, aminophenyl fluorescein assay (APF), and singlet oxygen sensor green assay (SOSG), respectively. Due to photobleaching, H_4TBB showed much weaker signals of type I ROSs than Zr-TBB (Figures S12−S14). Similarly, $^1O_2$ generation of H_4TBB reached a plateau within 1 min of light irradiation, while Zr-TBB showed a linear increase of $^1O_2$ signal throughout the 15 min experiment (Figure S15).

We next examined cellular uptake, *in vitro* ROS generation, and cytotoxicity of H_4TBB and Zr-TBB on 4T1 murine breast carcinoma cells. ICP-MS and UV−vis studies showed that 4T1 cells uptook significantly more Zr-TBB than H_4TBB (Figure S17). The *in vitro* generation of $O_2^{\bullet-}$, H_2O_2, $^{\bullet}OH$, and $^1O_2$ by Zr-TBB plus light irradiation [denoted Zr-TBB(+)] was detected under confocal laser scanning microscopy (CLSM) with superoxide detection, intracellular hydrogen peroxide, coumarin-3-carboxylic acid assay, and SOSG assay kits, respectively (Figure 3a). The generation of $^1O_2$ and $O_2^{\bullet-}$ by Zr-TBB(+) was confirmed by flow cytometric analyses. H_4TBB(+) generated much less ROSs than Zr-TBB(+), likely due to low cellular uptake, oxidation, and photobleaching. Zr-TBB(+) efficiently generated four different kinds of ROSs to facilitate type I and type II PDT. The cytotoxicity of Zr-TBB(+) was determined by MTS assay. Under normoxic condition, Zr-TBB(+) exhibited an IC_{50} of 0.91 ± 0.77 μM on 4T1 cells, while H_4TBB(+) did not show any cytotoxicity at ≤20 μM (Figure 3b). Under hypoxic condition, the IC_{50} values of Zr-TBB(+) and H_4TBB(+) on 4T1 cells were 2.94 ± 0.76 and 19.50 ± 0.82 μM, respectively (Figure 3c). The increased cytotoxicity of H_4TBB(+) under hypoxia likely resulted from reduced photobleaching at low O_2 concentration. The apoptosis of 4T1 cells after PDT treatments was evaluated by flow cytometry with annexin-V and propidium iodide staining. Zr-TBB(+)-treated cells gave significantly stronger apoptosis signals than those treated with H_4TBB(+) and PBS(+) (Figure S19). Flow cytometry and CLSM imaging

https://dx.doi.org/10.1021/jacs.0c02129
J. Am. Chem. Soc. 2020, 142, 7334−7339

studies also showed that Zr-TBB(+)-treated cells exhibited much stronger calreticulin (CRT) signals than those treated with H_4TBB(+) and PBS(+) (Figures S23 and S24), indicating more pronounced immunogenic cell death (ICD) caused by Zr-TBB(+).

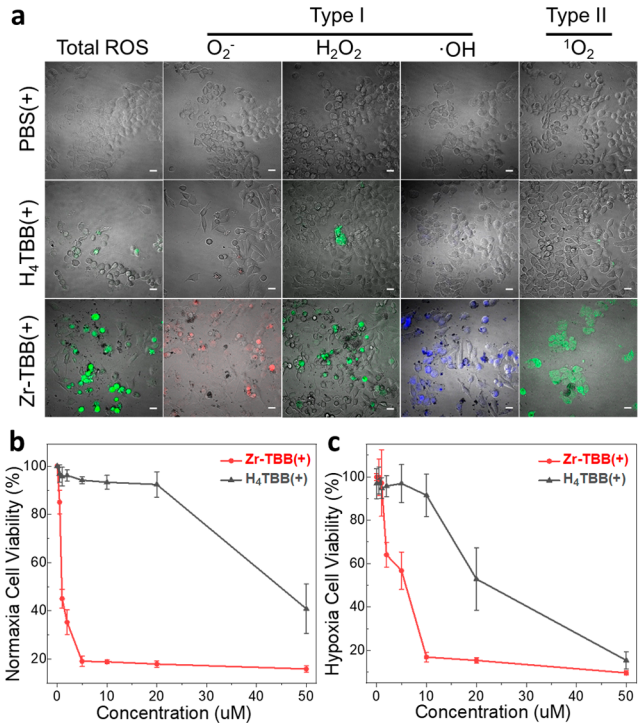

Figure 3. (a) CLSM images of various ROS species generated in 4T1 cells after light irradiation. Total ROS was detected by H_2DCFDA assay. Scale bar is 20 μm. (b, c) MTS assays of Zr-TBB(+) and H_4TBB(+) under normoxic (b) and hypoxic (c) conditions.

The *in vivo* antitumor efficacy was investigated on subcutaneous 4T1-bearing BALB/c mice and murine colon carcinoma MC38-bearing C57Bl/6 mice. Zr-TBB(+) exhibited excellent therapeutic effects to afford 91% tumor growth inhibition and a 40% cure rate on 4T1 model (Figure 4a) and 97% tumor growth inhibition and a 60% cure rate on MC38 model. H&E staining showed severe necrosis in Zr-TBB(+)-treated 4T1 tumors. TUNEL (Figure 4c) and CRT expression (Figure 4d) assays by CLSM showed strong apoptosis and ICD induced by Zr-TBB(+) treatment. Finally, steady body weight and minimal abnormalities of major organ sections indicated that Zr-TBB had no systematic toxicity on BALB/c and C57Bl/6 mice.

In summary, we report the use of the framework of Zr-TBB nMOF to stabilize bacteriochlorins toward oxygen and light irradiation. Zr-TBB mediated effective PDT by generating O_2^-, H_2O_2, $^{\bullet}$OH, and $^1O_2$ via both type I and type II mechanisms. Zr-TBB showed superb *in vivo* antitumor efficacy on mouse tumor models of breast and colon cancers to afford cure rates of 40% and 60%, respectively. nMOFs thus present a unique platform to design novel nanophotosensitizers based on bacteriochlorins and other unstable photosensitizing molecules.

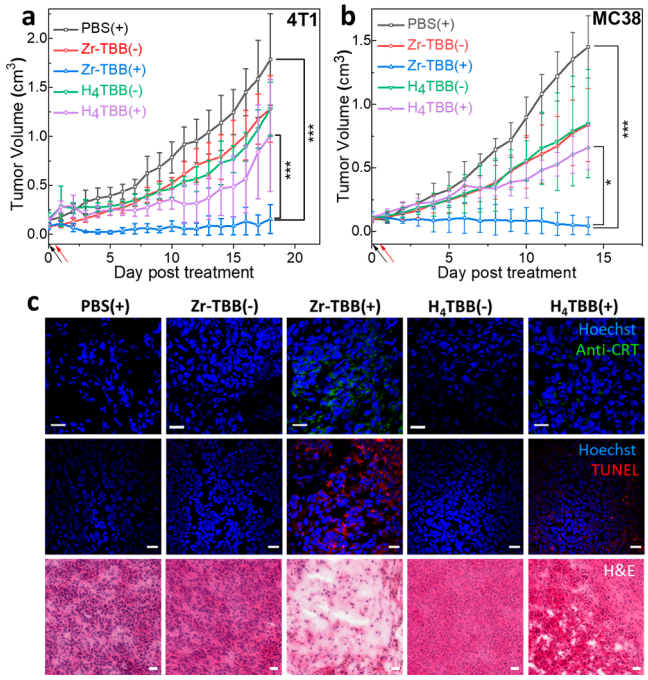

Figure 4. Antitumor efficacy on 4T1-bearing BALB/c mice (a) and MC38-bearing C57Bl/6 mice (b). (c) CLSM imaging of cell surface CRT (top) and cell apoptosis (middle) and H&E staining showing severe apoptosis and necrosis (bottom) after Zr-TBB(+) treatment on 4T1 tumors. Scale bar is 20 μm.

■ ASSOCIATED CONTENT

Supporting Information

The Supporting Information is available free of charge at https://pubs.acs.org/doi/10.1021/jacs.0c02129.

Synthesis and characterization of H4TBB and Zr-TBB, ROS generation and mechanism, anticancer efficacy, and DFT calculations (PDF)

Data for Hf-TBB single crystal (CIF)

■ AUTHOR INFORMATION

Corresponding Author

Wenbin Lin − *Department of Chemistry and Department of Radiation and Cellular Oncology and Ludwig Center for Metastasis Research, The University of Chicago, Chicago, Illinois 60637, United States;* orcid.org/0000-0001-7035-7759; Email: wenbinlin@uchicago.edu

Authors

Taokun Luo − *Department of Chemistry, The University of Chicago, Chicago, Illinois 60637, United States*

Kaiyuan Ni − *Department of Chemistry, The University of Chicago, Chicago, Illinois 60637, United States;* orcid.org/0000-0002-8152-6746

August Culbert − *Department of Chemistry, The University of Chicago, Chicago, Illinois 60637, United States*

Guangxu Lan − *Department of Chemistry, The University of Chicago, Chicago, Illinois 60637, United States;* orcid.org/0000-0002-0415-5849

Zhe Li − *Department of Chemistry, The University of Chicago, Chicago, Illinois 60637, United States*

Xiaomin Jiang − *Department of Chemistry, The University of Chicago, Chicago, Illinois 60637, United States;* orcid.org/0000-0001-8304-4938

https://dx.doi.org/10.1021/jacs.0c02129
J. Am. Chem. Soc. 2020, 142, 7334−7339

Michael Kaufmann − *Department of Chemistry, The University of Chicago, Chicago, Illinois 60637, United States*

Complete contact information is available at: https://pubs.acs.org/10.1021/jacs.0c02129

Author Contributions

[§]T.L. and K.N. contributed equally.

Notes

The authors declare no competing financial interest.

■ ACKNOWLEDGMENTS

We thank Yang Song, Xuanyu Feng, Yunhong Pi, and Wenbo Han for experimental help. We acknowledge the National Cancer Institute (U01-CA198989) and the University of Chicago Medicine Comprehensive Cancer Center (NIH CCSG: P30 CA014599) for funding support. NSF's ChemMatCARS Sector 15 is principally supported by the Divisions of Chemistry (CHE) and Materials Research (DMR), National Science Foundation, under Grant NSF/CHE-1834750. Use of the Advanced Photon Source, an Office of Science User Facility operated for the U.S. Department of Energy (DOE) Office of Science by Argonne National Laboratory, was supported by the U.S. DOE under Contract DE-AC02-06CH11357.

■ REFERENCES

(1) Lovell, J. F.; Liu, T. W.; Chen, J.; Zheng, G. Activatable photosensitizers for imaging and therapy. *Chem. Rev.* **2010**, *110* (5), 2839−2857.

(2) Luby, B. M.; Walsh, C. D.; Zheng, G. Advanced photosensitizer activation strategies for smarter photodynamic therapy beacons. *Angew. Chem., Int. Ed.* **2019**, *58* (9), 2558−2569.

(3) Huang, H.-C.; Mallidi, S.; Liu, J.; Chiang, C.-T.; Mai, Z.; Goldschmidt, R.; Ebrahim-Zadeh, N.; Rizvi, I.; Hasan, T. Photodynamic therapy synergizes with irinotecan to overcome compensatory mechanisms and improve treatment outcomes in pancreatic cancer. *Cancer Res.* **2016**, *76* (5), 1066−1077.

(4) Dolmans, D. E.; Fukumura, D.; Jain, R. K. Photodynamic therapy for cancer. *Nat. Rev. Cancer* **2003**, *3* (5), 380−387.

(5) Shao, S.; Rajendiran, V.; Lovell, J. F. Metalloporphyrin nanoparticles: Coordinating diverse theranostic functions. *Coord. Chem. Rev.* **2019**, *379*, 99−120.

(6) Lan, G.; Ni, K.; Xu, Z.; Veroneau, S. S.; Song, Y.; Lin, W. Nanoscale metal−organic framework overcomes hypoxia for photodynamic therapy primed cancer immunotherapy. *J. Am. Chem. Soc.* **2018**, *140* (17), 5670−5673.

(7) Hopper, C. Photodynamic therapy: a clinical reality in the treatment of cancer. *Lancet Oncol.* **2000**, *1* (4), 212−219.

(8) Mallidi, S.; Anbil, S.; Bulin, A.-L.; Obaid, G.; Ichikawa, M.; Hasan, T. Beyond the barriers of light penetration: strategies, perspectives and possibilities for photodynamic therapy. *Theranostics* **2016**, *6* (13), 2458.

(9) Chen, Y.; Li, G.; Pandey, R. K. Synthesis of bacteriochlorins and their potential utility in photodynamic therapy (PDT). *Curr. Org. Chem.* **2004**, *8* (12), 1105−1134.

(10) Zhou, Z.; Song, J.; Nie, L.; Chen, X. Reactive oxygen species generating systems meeting challenges of photodynamic cancer therapy. *Chem. Soc. Rev.* **2016**, *45* (23), 6597−6626.

(11) Lan, G.; Ni, K.; Veroneau, S. S.; Feng, X.; Nash, G. T.; Luo, T.; Xu, Z.; Lin, W. Titanium-Based Nanoscale Metal−Organic Framework for Type I Photodynamic Therapy. *J. Am. Chem. Soc.* **2019**, *141* (10), 4204−4208.

(12) Azzouzi, A.-R.; Vincendeau, S.; Barret, E.; Cicco, A.; Kleinclauss, F.; van der Poel, H. G.; Stief, C. G.; Rassweiler, J.; Salomon, G.; Solsona, E.; Alcaraz, A.; Tammela, T. T.; Rosario, D. J.; Gomez-Veiga, F.; Ahlgren, G.; Benzaghou, F.; Gaillac, B.; Amzal, B.; Debruyne, F. M. J.; Fromont, G.; Gratzke, C.; Emberton, M. Padeliporfin vascular-targeted photodynamic therapy versus active surveillance in men with low-risk prostate cancer (CLIN1001 PCM301): an open-label, phase 3, randomised controlled trial. *Lancet Oncol.* **2017**, *18* (2), 181−191.

(13) Pucelik, B.; Arnaut, L. G.; Stochel, G.; Dąbrowski, J. M. Design of Pluronic-Based Formulation for Enhanced Redaporfin-Photodynamic Therapy against Pigmented Melanoma. *ACS Appl. Mater. Interfaces* **2016**, *8* (34), 22039−22055.

(14) Huang, Y. Y.; Balasubramanian, T.; Yang, E.; Luo, D.; Diers, J. R.; Bocian, D. F.; Lindsey, J. S.; Holten, D.; Hamblin, M. R. Stable synthetic bacteriochlorins for photodynamic therapy: role of dicyano peripheral groups, central metal substitution (2H, Zn, Pd), and Cremophor EL delivery. *ChemMedChem* **2012**, *7* (12), 2155−2167.

(15) Dąbrowski, J. M.; Arnaut, L. G. Photodynamic therapy (PDT) of cancer: from local to systemic treatment. *Photochem. Photobiol. Sci.* **2015**, *14* (10), 1765−1780.

(16) Grahn, M. F.; McGuinness, A.; Benzie, R.; Boyle, R.; de Jode, M. L.; Dilkes, M. G.; Abbas, B.; Williams, N. S. Intracellular uptake, absorption spectrum and stability of the bacteriochlorin photosensitizer 5, 10, 15, 20-tetrakis (m-hydroxyphenyl) bacteriochlorin (mTHPBC). Comparison with 5, 10, 15, 20-tetrakis (m-hydroxyphenyl) chlorin (mTHPC). *J. Photochem. Photobiol., B* **1997**, *37* (3), 261−266.

(17) Huang, L.; Huang, Y.-Y.; Mroz, P.; Tegos, G. P.; Zhiyentayev, T.; Sharma, S. K.; Lu, Z.; Balasubramanian, T.; Krayer, M.; Ruzié, C.; et al. Stable synthetic cationic bacteriochlorins as selective antimicrobial photosensitizers. *Antimicrob. Agents Chemother.* **2010**, *54* (9), 3834−3841.

(18) Pandey, R. K.; Constantine, S.; Tsuchida, T.; Zheng, G.; Medforth, C. J.; Aoudia, M.; Kozyrev, A. N.; Rodgers, M. A. J.; Kato, H.; Smith, K. M.; Dougherty, T. J. Synthesis, photophysical properties, *in vivo* photosensitizing efficacy, and human serum albumin binding properties of some novel bacteriochlorins. *J. Med. Chem.* **1997**, *40* (17), 2770−2779.

(19) Furukawa, H.; Cordova, K. E.; O'Keeffe, M.; Yaghi, O. M. The chemistry and applications of metal-organic frameworks. *Science* **2013**, *341* (6149), 1230444.

(20) Chen, B.; Xiang, S.; Qian, G. Metal− organic frameworks with functional pores for recognition of small molecules. *Acc. Chem. Res.* **2010**, *43* (8), 1115−1124.

(21) Long, J. R.; Yaghi, O. M. The pervasive chemistry of metal−organic frameworks. *Chem. Soc. Rev.* **2009**, *38* (5), 1213−1214.

(22) Liu, C.; Zeng, C.; Luo, T.-Y.; Merg, A. D.; Jin, R.; Rosi, N. L. Establishing porosity gradients within metal−organic frameworks using partial postsynthetic ligand exchange. *J. Am. Chem. Soc.* **2016**, *138* (37), 12045−12048.

(23) Fateeva, A.; Chater, P. A.; Ireland, C. P.; Tahir, A. A.; Khimyak, Y. Z.; Wiper, P. V.; Darwent, J. R.; Rosseinsky, M. J. A Water-Stable Porphyrin-Based Metal−Organic Framework Active for Visible-Light Photocatalysis. *Angew. Chem.* **2012**, *124* (30), 7558−7562.

(24) Shustova, N. B.; Cozzolino, A. F.; Dincă, M. Conformational locking by design: Relating strain energy with luminescence and stability in rigid metal−organic frameworks. *J. Am. Chem. Soc.* **2012**, *134* (48), 19596−19599.

(25) Lan, G.; Ni, K.; Lin, W. Nanoscale metal−organic frameworks for phototherapy of cancer. *Coord. Chem. Rev.* **2019**, *379*, 65−81.

(26) Lu, K.; He, C.; Guo, N.; Chan, C.; Ni, K.; Weichselbaum, R. R.; Lin, W. Chlorin-based nanoscale metal−organic framework systemically rejects colorectal cancers via synergistic photodynamic therapy and checkpoint blockade immunotherapy. *J. Am. Chem. Soc.* **2016**, *138* (38), 12502−12510.

(27) Ni, K.; Aung, T.; Li, S.; Fatuzzo, N.; Liang, X.; Lin, W. Nanoscale metal-Organic framework mediates radical therapy to enhance cancer immunotherapy. *Chem.* **2019**, *5* (7), 1892−1913.

(28) Ni, K.; Luo, T.; Lan, G.; Culbert, A.; Song, Y.; Wu, T.; Jiang, X.; Lin, W. A Nanoscale Metal−Organic Framework to Mediate Photodynamic Therapy and Deliver CpG Oligodeoxynucleotides to

Enhance Antigen Presentation and Cancer Immunotherapy. *Angew. Chem.* **2020**, *132* (3), 1124−1128.
(29) Pereira, M. M.; Monteiro, C. J. P.; Simões, A. V. C.; Pinto, S. M. A.; Abreu, A. R.; Sá, G. F. F.; Silva, E. F. F.; Rocha, L. B.; Dąbrowski, J. M.; Formosinho, S. J.; Simões, S.; Arnaut, L. G. Synthesis and photophysical characterization of a library of photostable halogenated bacteriochlorins: an access to near infrared chemistry. *Tetrahedron* **2010**, *66* (49), 9545−9551.
(30) Ghosh, A. Theoretical Comparative Study of Free Base Porphyrin, Chlorin, Bacteriochlorin, and Isobacteriochlorin: Evaluation of the Potential Roles of ab Initio Hartree− Fock and Density Functional Theories in Hydroporphyrin Chemistry. *J. Phys. Chem. B* **1997**, *101* (16), 3290−3297.
(31) Bashkatov, A. N.; Berezin, K. V.; Dvoretskiy, K. N.; Chernavina, M. L.; Genina, E. A.; Genin, V. D.; Kochubey, V. I. Measurement of tissue optical properties in the context of tissue optical clearing. *J. Biomed. Opt.* **2018**, *23* (9), 091416.
(32) Feng, D.; Chung, W.-C.; Wei, Z.; Gu, Z.-Y.; Jiang, H.-L.; Chen, Y.-P.; Darensbourg, D. J.; Zhou, H.-C. Construction of ultrastable porphyrin Zr metal−organic frameworks through linker elimination. *J. Am. Chem. Soc.* **2013**, *135* (45), 17105−17110.
(33) Stratonnikov, A. A.; Meerovich, G. A.; Loschenov, V. B. Photobleaching of photosensitizers applied for photodynamic therapy. *Optical Methods for Tumor Treatment and Detection: Mechanisms and Techniques in Photodynamic Therapy IX*; International Society for Optics and Photonics: 2000; pp 81−91.
(34) Bonnett, R.; Martínez, G. Photobleaching of compounds of the 5, 10, 15, 20-Tetrakis (m-hydroxyphenyl) porphyrin Series (m-THPP, m-THPC, and m-THPBC). *Org. Lett.* **2002**, *4* (12), 2013−2016.
(35) Bonnett, R.; Martınez, G. Photobleaching of sensitisers used in photodynamic therapy. *Tetrahedron* **2001**, *57* (47), 9513−9547.
(36) Silva, E. F.; Serpa, C.; Dąbrowski, J. M.; Monteiro, C. J.; Formosinho, S. J.; Stochel, G.; Urbanska, K.; Simões, S.; Pereira, M. M.; Arnaut, L. G. Mechanisms of singlet-oxygen and superoxide-ion generation by porphyrins and bacteriochlorins and their implications in photodynamic therapy. *Chem. - Eur. J.* **2010**, *16* (30), 9273−9286.

https://dx.doi.org/10.1021/jacs.0c02129
J. Am. Chem. Soc. 2020, 142, 7334−7339